LA-UR- 09-00780

Approved for public release;
distribution is unlimited.

Title:	In vivo breast sound-speed imaging with ultrasound tomography
Author(s):	Lianjie Huang, EES-17 Cuiping Li, Neb Duric, and Peter Littrup, Karmanos Cancer Institute
Intended for:	Ultrasound in Medicine and Biology

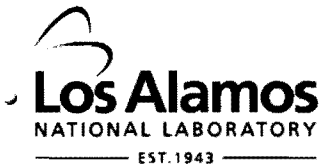

Form 836 (7/06)

In vivo breast sound-speed imaging with ultrasound tomography

Cuiping Li

Karmanos Cancer Institute, 110 East Warren, Hudson-Webber Cancer Research Center, Detroit, MI 48201. Phone: 313-576-8768 Email: lic@karmanos.org

Nebojsa Duric

Karmanos Cancer Institute, 110 East Warren, Hudson-Webber Cancer Research Center, Detroit, MI 48201. Phone: 313-576-8706 Email: duric@karmanos.org

Peter Littrup

Karmanos Cancer Institute, 110 East Warren, Hudson-Webber Cancer Research Center, Detroit, MI 48201. Phone: 313-576-8721 Email: littrupp@karmanos.org

Lianjie Huang

MS D443, Los Alamos National Laboratory, Los Alamos, NM 87545. Phone: 505-665-1108 Email: ljh@lanl.gov

ABSTRACT

We discuss a bent-ray ultrasound tomography algorithm with total-variation (TV) regularization. We have applied this algorithm to 61 *in vivo* breast datasets collected with our in-house clinical prototype for imaging sound-speed distributions in the breast. Our analysis showed that TV regularization could preserve sharper lesion edges than the classic Tikhonov regularization. Furthermore, the image quality of our TV bent-ray sound-speed tomograms was superior to that of the straight-ray counterparts for all types of breasts within BI-RADS density categories 1-4. For all four breast types from fatty to dense, the improvements for average sharpness (in the unit of $(m \cdot s)^{-1}$) of lesion edges in our TV bent-ray tomograms are between 2.1 to 3.4 fold compared to the straight ray tomograms. Reconstructed sound-speed tomograms illustrated that our algorithm could successfully image fatty and glandular tissues within the breast. We calculated the mean sound-speed values for fatty tissue and breast parenchyma as $1422 \pm 9\, m/s$ (mean $\pm$ SD) and $1487 \pm 21\, m/s$, respectively. Based on 32 lesions in a cohort of 61 patients, we also found that the mean sound-speed for malignant breast lesions ($1548 \pm 17\, m/s$) was higher, on average, than that of benign ones ($1513 \pm 27\, m/s$) (one-sided $p<0.001$). These results suggest that, clinically, sound-speed tomograms can be used to assess breast density (, and therefore, breast cancer risk), as well as detect and help differentiate breast lesions. Finally, our sound-speed tomograms may also be a useful tool to monitor the clinical response of breast cancer patients to neo-adjuvant chemotherapy.

Key words: Ultrasound tomography, Total-variation, Sound-speed, Breast imaging.

INTRODUCTION

Breast cancer affects one in eight women during their lives, making it the most common cancer and the second most common cause of cancer death after lung cancer. Although its false positive and false negative rates are high, mammography is still the current gold standard screening tool for breast cancer. Currently, conventional ultrasound is only an adjunct technique to mammography for breast cancer diagnosis due to its highly operator dependent nature and inconsistency in detecting some early cancers. Numerous ongoing studies (Kolb et al. 2002; Lucas-Fehm 2005) including the large ACRIN study (ACRIN: http://www.acrin.org, 2008) have been aimed at evaluating ultrasound (US) for breast cancer screening. Most of the early experimental work to develop breast ultrasound computed tomography (UCT) was performed in late 70's and early 80's (Greenleaf et al., 1974, 1977, 1981, 1987; Carson et al. 1981; Schreiman et al., 1984; Scherzinger et al, 1989). Since the early investigators were often hindered by the limited memory and processor speed of their computers, the quality of the reconstruction images was not high enough for clinical use (Jones, 1993). As Andre et al. note in their paper (1997), after the initial experimental research, most of the work on UCT through the mid 1990's involved theoretical reconstructions and not experimental designs. Rapidly improving computer power allowed investigators to explore *in vivo* applications of breast ultrasound tomography. Examples include the work of Carson et al (1981), Andre et al (1997), Johnson et al (1999), Marmarelis et al (2002), Liu and Waag (1997), Duric et al (2005, 2007). Chang et al. (2007) also applied limited-angle UCT to clinical breast radio-frequency (RF) signals collected by conventional B-mode ultrasound machine.

There are basically two types of UCT methods. The first is based on ray theory, which is fast and stable. The second applies inverse scattering principles, which are much more time

consuming but have higher resolution (Devaney, 1981, 1982; Johnson et al., 1983, 1999). For ray-theory based breast UCT, there are primarily two modes. The first mode uses the time-of-flight measurements of the transmission US signals to reproduce the sound-speed distribution within the breast. The second mode reconstructs attenuation measurements to give a distribution of energy absorption and scatter within the breast. Our study focuses on the first mode in order to improve the quality of UCT by overcoming the shortcomings of previous non-iterative straight-ray mathematical models, thereby making it more clinically acceptable for *in vivo* breast imaging.

Based on Fermat's Principle and Snell's Law, the ultrasound ray path in an inhomogeneous medium (such as breast tissue) is not straight, which makes the inverse problem nonlinear. The first bent-ray ultrasound tomography was proposed by Schomberg in 1978. However, applications of bent-ray algorithm were limited to numerical simulations and phantom studies thereafter (Norton, 1987; Andersen, 1987, 1990). To record both the transmitted and reflected ultrasound energy, a clinical ultrasound ring array scanner for breast cancer diagnosis, termed Computed Ultrasound Risk Evaluation (CURE), was designed and built at the Karmanos Cancer Institute (KCI), Detroit, MI (Duric et al., 2005, 2007; Littrup et al. 2001, 2002). Since most abnormal breast lesions have higher sound-speed than normal breast tissue (Gauss et al., 1997), the goal is to accurately and efficiently produce images of breast sound-speeds based on the ultrasound signals that are transmitted through the breast tissue to the other side of the ring array. Therefore, a robust ultrasound sound-speed tomography algorithm is critical to ensure a high-resolution sound-speed tomogram of the breast data.

In this study, we present an iterative bent-ray ultrasound tomography method to extract sound-speed information from *in vivo* ultrasound breast data acquired by CURE. We investigate

the use of total-variation (TV) to regularize the uneven ray coverage, which leads to a non-quadratic minimization problem. The TV method was introduced by Rudin et al in 1992 and has been widely used in inverse problems in image processing (denoising, restoration and zooming). While most regularization methods, such as Tikhonov regularization, tend to smooth reconstructed images, TV regularization preserves edge information. We applied a limited memory Broyden-Fletcher-Goldfarb-Shanno (L-BFGS) method to solve the optimization problem (Nocedal and Wright, 2000). Sixty-one datasets from clinical breast patients were acquired by CURE and reconstructed using this algorithm.

The paper is organized as follows. Patient selection and the CURE device are briefly described, followed by details of the iterative tomography algorithm and applications to clinical breast data. Finally, the potential clinical value of the reconstructed sound-speed images and their limitations are addressed.

MATERIALS AND METHODS

Patient Selection

A total of 61 patients with a variety of breast types, breast mass types and sizes, were included in this study. Patient recruitment was done by a research nurse at our Comprehensive Breast Center. All patients were scanned with our clinical UCT, or CURE, prototype after mammography and standard US exams, but before US guided biopsy. Scanning procedures were performed under an institutional review board approved protocol and in compliance with the Health Insurance Portability and Accountability Act (HIPAA). CURE data was not used for any clinical decisions and reviewed only after the patient had left KCI.

The CURE Device and Data Collection

The CURE device is a clinical prototype producing near real time data acquisition and integrated into the normal patient flow of the Comprehensive Breast Center. A detailed description of CURE was presented by Duric et al. (2007), and a brief overview is given below.

Figure 1a is a schematic representation of the CURE ring transducer. The 20-cm-diameter ring consists of 256 equally-spaced and water-coupled transducers, immersed in a water tank (Fig. 1a). During the scan, the patient is positioned prone with the breast situated through a hole in the canvas bedding. The breast is suspended in water, inside the imaging tank, and encircled by the ring. A motorized gantry translates the ring in the vertical direction, starting from the chest wall through the breast's nipple region. One complete scan takes about 1 minute, and leads to approximately 75 slices of data per patient.

During scanning at each step, all 256 transducer elements sequentially emit a fan beam of ultrasound signals with a central frequency of 1.5 MHz toward the opposite side of the ring. The scattered (transmission) and backscattered (reflection) ultrasound signals are subsequently recorded by all 256 elements at a sampling rate of 6.25 MHz. Figure 1b (from Duric et al 2007) illustrates that the ring insonofies a cross-section of the breast which leads to data of all wavefields (including both transmission and reflection) that can be used to reconstruct images of acoustic properties.

Ultrasound Sound-speed Tomography

Based on the Radon transform, classical tomography reconstruction using Filtered back-projection (FBP) cannot take ray bending into account. However, according to Fermat's Principle and Snell's Law, the ultrasound ray path is not straight in an inhomogeneous medium

like breast tissue, which makes the inverse problem nonlinear. In this study, an iterative bent-ray ultrasound tomography algorithm with a TV regularization term was assessed. To solve the bent-ray ultrasound tomography problem, a regular rectangular grid model was created on the image plane, whose boundaries enclose the transducer ring (Fig. 2). During each iteration, both the forward problem and the inverse problem were solved, and the sound-speed model was updated for successive iterations. Details about our methods to solve forward and inverse problems are described as follows.

Forward Modeling

2-D ultrasound wave propagation is governed by the eikonal equation

$$(\nabla E)^2 = (\partial T/\partial x)^2 + (\partial T/\partial y)^2 = (1/v)^2 = (s_x^2 + s_y^2), \quad (1)$$

where T is the travel-time, v is the sound-speed, and (s_x, s_y) is the slowness vector of the ultrasound wave that is defined as the inverse of sound-speed. In eq. (1), $E = const.$ describes the 'wavefronts', and 'rays' are defined as the orthogonal trajectories of these wavefronts.

In this paper, eq. (1) was solved using Klimes' grid travel-time tracing technique (1996), which had been proven to be both accurate and fast. Klimes' method calculates the slowness vector (s_x, s_y) and travel-time T at the center point of each grid cell simultaneously with at least second-order accuracy (relative to the grid spacing). (s_x, s_y) and T at an arbitrary point within the grid model were interpolated by 2-D fourth order Lagrange interpolation. An ultrasound ray was backpropagated from receiver to transmitter in the following way:

(1) Starting from the receiver location (x_r, y_r), the ray segment within the current grid cell was traced along the direction $\bar{G} = (-s_{x_r}, -s_{y_r})$ until it intercepted the cell boundary at point (x_i, y_i);

(2) Update $\bar{G}$ to be the negative slowness vector of the intercept point $\bar{G} = (-s_{x_i}, -s_{y_i})$, and trace the ray segment within the next adjacent cell;

(3) Repeat (2), until the current ray arrives at the transmitter within a certain tolerance.

Assuming that the slowness is constant within each grid cell, the bent ray path can be traced using the above procedure fairly accurately. An illustration of the grid model and the backpropagated is shown in Fig. 2.

Inverse Problem

Let Δt_i be the difference between the *ith* picked time-of-flight (TOF) for the recorded ultrasound data and the *ith* calculated TOF for the sound-speed model, our inverse problem can be described as follows

$$\sum_{j}^{M} l_{ij} \Delta s_j = \Delta t_i \,, \tag{2}$$

where Δs_j is the slowness perturbation for the *jth* grid cell, which needs to be inverted, and l_{ij} is the ray length of the *ith* ray within the *jth* cell. Equation (2) can be expressed as a matrix form

$$L\Delta S = \Delta T \,. \tag{3}$$

This is a nonlinear inverse problem due to ray bending. The objective function for the inverse problem can be described as in eq. (4)

$$f = \arg\min_{\Delta S}(\| L\Delta S_\lambda - \Delta T \|^2 + \lambda TV(\Delta S_\lambda)) \,, \tag{4}$$

and

$$TV(\Delta S_\lambda) = \iint \sqrt{|\nabla(\Delta S_\lambda)|^2}\, dxdy. \tag{5}$$

However, $TV(\Delta S_\lambda))$ is not differentiable at zero. So in order to avoid this difficulty a small positive constant value is added to the equation (6)

$$TV(\Delta S_\lambda) = \iint \sqrt{|\nabla(\Delta S_\lambda)|^2 + \beta^2}\, dxdy. \tag{6}$$

The quantity $\sqrt{|\nabla(\Delta S_\lambda)|^2 + \beta^2}$ is known as the gradient magnitude. This provides us with the information about the discontinuities in the image. In eq. (4), λ is the regularization parameter that balances the roughness of the inverted results and the fit to the data.

To avoid direct computation of Hessian matrices, we applied the quasi-Newton algorithm—limited memory Bryoyden-Fletcher-Goldfarb-Shanno (LBFGS) method to iteratively solve the nonlinear problem in eq. (4) for ΔS, starting with a homogeneous sound-speed model (algorithm available at: http://www.alglib.net/optimization/lbfgs.php). The LBFGS method was proven to be both time and memory efficient (Nocedal et al., 2000). After each iteration, an updated sound-speed model was obtained by adding the solution ΔS to the initial model. Rays were traced on the updated model using the method discussed in the forward modeling section, and the TOF data were updated at the same time. The iteration continues until the TOF misfit ΔT was not significantly improved from the previous iteration, which meant the solutions had converged. The regularization parameter λ was determined using the L-curve technique (refer to Hansen's paper for details, available at http://www.math/sintef.no/vskoler/2005/notes/Lcurve.pdf).

In this study, we applied our TV bent-ray tomography algorithm to a total of 61 *in vivo* breast datasets. Uncertainties in the sound-speed tomograms were simply estimated by calculating the standard deviation in reconstructions for water shot data. Water shot data was recorded before

each patient scan, with only water in the tank. Sixteen reconstructions with 1 *mm* by 1 *mm* grid cell for water shot data were used to do the analysis. The typical standard deviation for the sound-speed values in water was $4\ m/s$ per pixel.

Our clinical protocol was designed to include a sample of patients with a wide variety of breast types, ranging from fatty to dense on the BI-RADS categories 1-4. The sound-speed tomograms were reviewed and classified by a board certified radiologist with over 10 years of breast imaging experience (PJL).

Define sharpness of lesion edges

In order to define sharpness of lesion edges in a more illustrative way, we took the TV tomogram in Fig. 3a as an example: (1) selecting a region-of-interest (ROI) by drawing an ellipse enclosing the lesion (solid ellipse in Fig. 3a), and the sound-speed outside the ROI is set to zero, (2) select another ROI inside the ROI in (1) (dashed ellipse in Fig. 3a), (3) calculate the mean background sound-speed (BgSS) using those pixels inside the solid ellipse but outside the dashed ellipse, (4) find the maximum sound-speed (MaxSS) inside the dashed ellipse, and calculate the half-power (HpSS) sound-speed between background (BgSS) and the maximum sound-speed (HpSS=BgSS+(MaxSS-BgSS)/2), (5) threshold the image obtained in (1) with BgSS and HpSS, respectively, then subtract the two resulting images (Fig. 3d), (6) the edge sharpness is defined as: (HpSS – BgSS)/(number of pixels in the subtracted image in Fig. 3d). The unit for the sharpness obtained in the above way is $(m \cdot s)^{-1}$.

Select region of interest (ROI)

Two methods were used to isolate lesions in the sound-speed tomograms as described in the following.

The first method utilizes CURE reflection images for regions of interest (ROI) selection at the lesion locations. Since CURE reflection images were reconstructed from the same data as sound-speed images, they can be registered without any geometric discrepancies. Figure 4a shows a typical sound-speed tomogram, with an invasive ductal carcinoma at 12:00 to 1:00 o'clock. The reflection image in Fig. 4b for the same slice has a clear edge for the lesion and the ROI within the enclosed curve was manually selected. A plugin for ImageJ that was developed in-house was used to record a mask image with all 1's within the selected ROI and all 0's outside the ROI. The sound-speed tomogram in Fig. 4a was multiplied by the mask image, and the resulting image is shown in Fig. 4c with all 0's except that the original sound-speed values are unchanged within the ROI.

The second method was used to select an ROI when there was no clear lesion edge in the reflection image. In this method the half-power sound-speed (HpSS) is calculated following those steps as described in the section "*Define sharpness of lesion edges*". The ROI is selected by thresholding the sound-speed image obtained in step (1) with HpSS. This ROI selection method was also applied to the sound-speed image in Fig. 4a, and the resulting image (Fig. 4d) is put next to the one obtained by referring to reflection image (Fig. 4c) for visual comparison.

RESULTS

Total-variation (L1-norm)) regularization vs. Tikhonov (L2-norm) regularization

We compared the TV sound-speed tomograms (third iteration) to those reconstructed with the classic Tikhonov regularization (third iteration). Fig. 3 shows a TV tomogram (a), Tikhonov

tomogram (b), and sound-speed cross-sections (c) along the solid line from the TV tomogram and along the dashed line in Tikhonov tomogram. The breast in Fig. 3 has a 55 x 47 x 37 mm invasive ductal carcinoma at 12:00 to 1:00 o'clock. Note that the TV method not only preserved shaper edges of the lesion, but also damped out the "ray" artifacts more than the Tikhonov method. For fair comparison, the two tomograms in Fig. 3 are shown in the same absolute sound-speed scale ranging from 1350 m/s to 1600 m/s.

To quantitatively illustrate the edge-preserving property of the TV regularization, we calculated the sharpness of lesion edges for tomograms in Fig. 3a and 3b according to the method described in the *"Define sharpness of lesion edges"* section. The obtained sharpness for the lesion in Fig. 3a (TV reconstruction) is 0.094 $(m \cdot s)^{-1}$, while the sharpness for the lesion in Fig. 3b (Tikhonov reconstruction) is $0.039(m \cdot s)^{-1}$. The improvement for TV reconstruction is about 2.4 times over the Tikhonov reconstruction.

Bent-ray inversion vs. straight-ray inversion

We also compared TV bent-ray sound-speed tomograms for *in vivo* data with their straight-ray counterparts. Our analysis showed that, for our selected patients, the TV bent-ray approach led to sharply improved image quality (i.e. lesion sharpness). In vivo examples are used to illustrate this point.

In Fig. 5 through Fig. 8, we show four examples to demonstrate the improvements of the TV bent-ray reconstructions for breasts of different densities. For fair comparisons, the TV bent-ray tomograms and the straight-ray tomograms are shown in the same absolute sound-speed scale from 1350 m/s to 1550 m/s. In all four figures, (a) are the TV bent-ray inversions (third iteration), (b) are the straight-ray inversions, and (c) are sound-speed cross-sections along the

solid line in (a) (upper panel) and the dashed line in (b) (lower panel). Arrows in all four figures indicate the lesion locations. A fibroadenoma within a fatty breast is shown in Fig. 5. The TV bent-ray inversion exhibited higher resolution and sharper lesion edge than the straight-ray inversion. Figure 6 shows a high sound-speed mass at the 2:00 o'clock position in a patient with scattered breast density, which was pathologically confirmed as a 4.8 x 1.7 x 2.9 cm invasive carcinoma. The sound-speed and position tracings for the TV bent-ray image (fig 6c-top) confirm a significantly higher sound-speed for the mass (mean=1553 *m/s*) than the adjacent water in the bath (mean=1498 *m/s*; one-sided $p<<0.001$). Whereas the straight-ray image (fig 6c-bottom) shows no significant sound-speed differences between the tumor and adjacent water (mean=1491 *m/s* vs 1488 *m/s*; one-sided $p>0.19$). Figure 7 shows a heterogeneous breast with an invasive ductal carcinoma at 10:00 o'clock. Compared to the straight-ray inversion (Fig. 7b), the TV bent-ray inversion in Fig. 7a again shows more sharply defined structures within the breast, whereby there is significantly higher sound-speed over adjacent water in the mass (mean=1565 *m/s* vs 1507 *m/s*; $p<<0.001$). The dense breast shown in Fig. 8 shows a 1.6 x 1.1 x 1.8 cm fibroadenoma in the 2:00 o'clock position. The higher contrast for the fibroadenoma is confirmed by the sound-speed tracing (Fig. 8a&(c-upper), effectively making it much more clinically discernible than the straight-ray inversion 8b&(c-lower)). Again, the straight-ray tomogram has the mass sound-speed insignificantly different than from the adjacent water, literally washing out the image. In this paper, p-values were calculated using a one-sided z-test.

Sound-speeds of the lesions are also illustrated in their cross-sections (Fig. 5c through Fig. 8c), where the lesions are indicated by arrows. The edge sharpness for all four lesions was calculated as described in the section "*Define sharpness of lesion edges*", and is presented in

Table 1. The ratios of the calculated sharpness between the TV bent-ray reconstructions and straight-ray reconstructions for breasts in Fig. 5 through 8 are 2.5, 2.3, 2.1 and 3.4, respectively.

Fatty tissue vs. breast parenchyma

Breast density is a known risk factor for developing breast cancer. Breast density is determined by the ratio of breast parenchyma to fatty tissue within the breast. Separation of fatty tissue from breast parenchyma would be a significant step for breast density evaluation using our sound-speed tomograms (Glide et al., 2007; Glide-Hurst et al., 2008). Examples of sagittal views of four breasts within the BI-RAD categories 1-4 are presented in Fig. 9, where the breast parenchyma (in light color) is clearly discernible from fatty tissue (in dark color). These sagittal sound-speed tomograms were generated by reslicing the coronal sound-speed stacks in ImageJ, and illustrated in the same absolute sound-speed scale from 1350 *m/s* to 1550 *m/s*.

We utilized the k-mean clustering routine of ImageJ (an open source package available at http://rsb.info.nih.gov/ij) to segment the sound-speed tomograms for a cohort of 61 patients. To reduce workload, we segmented every 10th sound-speed tomogram for each patient. Since the abnormal lesions were not considered part of the normal breast architecture, we removed them from the sound-speed tomograms before we applied the clustering. Details of k-mean clustering segmentation are described by Glide et al. (2007). For more quantitative comparison, we calculated the mean sound-speeds for fatty tissue and breast parenchyma based on these segmentation results. The calculated mean sound-speeds were $1422 \pm 9\, m/s$ (mean $\pm$ SD) and $1487 \pm 21\, m/s$ for fatty tissue and breast parenchyma (one-sided $p<<0.001$), respectively (Table 2).

Benign vs. malignant lesions

Out of 32 lesions in 61 patients, 19 were malignant (16 invasive ductal carcinoma (IDC) and 3 ductal carcinoma in situ (DCIS)) and 13 were benign (8 fibroadenoma and 5 cysts, complicated cysts or fibrocystic structures). We selected the slices that contained lesions based on Radiologists' evaluations. We isolated lesions using the methods discussed in the section "*Select region of interest (ROI).*" Of a total 32 lesions, 20 were isolated with the first method and 12 were isolated using the second method. The mean sound-speed of a lesion for a single patient was calculated by summing all sound-speeds for every pixel within the ROI in the selected slices, then dividing this summation by the total number of pixels. To avoid bias because of different ROI selection methods, we compared the mean sound-speeds for benign and malignant lesions for the above two groups (Table 3). No systematic difference was seen between these two ROI selection methods. Mean sound-speed histograms for 13 benign lesion and 19 malignant lesions are depicted in Fig. 10, where malignant lesions show, on average, higher mean sound-speed than benign lesions. As presented in Table 2, the mean sound-speeds for malignant and benign lesions were $1548 \pm 17\, m/s$ and $1513 \pm 27\, m/s$ (one-sided $p<0.001$), respectively.

DISCUSSION

Comparison in Fig. 3 makes it clear that the TV reconstruction is superior to the reconstruction obtained with the classic Tikhonov regularization. Although TV is computationally more intensive than Tikhonov reconstruction, Vogel et al (1998) demonstrated that this difference was not significant. Our own experience suggests that reconstruction time for TV and Tikhonov regularization are about the same. We also compared *in vivo* TV bent-ray

tomograms with their straight-ray counterparts. These comparisons (Fig. 5 to Fig. 8, especially the cross-section plots from Fig. 5c through 8c) clearly showed that the TV bent-ray tomograms exhibited more tissue structures within the breast than their straight-ray counterparts. It was also obvious that the straight-ray tomograms were strongly degraded relative to the TV bent-ray tomograms because the linear approximation in straight-ray tomography was not accurate enough for the non-linear inverse problem. For our TV bent-ray tomograms (Fig. 5 through Fig. 8), there were improvements for average sharpness of lesion edges seen in all four breasts from fatty to dense. Perhaps more importantly, the improved contrast in the TV bent-ray tomograms leads to significantly greater enhancement of the masses relative to the background. Also, our results on mean sound-speeds of benign ($1513 \pm 27\, m/s$) and malignant lesions ($1548 \pm 17\, m/s$) generally corresponds with those reported in literature. Duck (1990) has calculated the mean sound-speeds for carcinoma and fibroadenoma to be $1584 \pm 27\, m/s$ and $1550 \pm 32\, m/s$, respectively. Chang (2007) reports a mean sound-speed of $1499.8 \pm 26.8\, m/s$ for fibroadenoma and a mean sound-speed of $1530.9 \pm 36.2\, m/s$ for carcinoma.

The results of our study suggest three potential clinical applications for our TV bent-ray algorithm. These all require the most accurate differentiation of focal areas that have different sound-speeds, including tracking them over time as a means to potentially reduce overall x-ray exposure to the breast. First, our sound-speed tomograms may be used to assess breast density. Second, they can help to detect and characterize breast lesions. Third, they also can be used to monitor clinical response of breast cancer patients to neo-adjuvant chemotherapy. We now discuss each of these applications.

Breast density is an important risk factor for developing breast cancer. Studies have shown that women with high mammographic breast density are at higher risk of developing breast

cancer (Boyd et. al., 1995, 2002; Wolfe, et. al., 1987; Hall, 2008). We have previously shown (Glide et al., 2007; Glide-Hurst et al., 2008) a definite positive correlation (Pearson correlation coefficient=0.87) between mean sound-speed values and breast density. From fatty to dense breasts, the mean sound-speed values tend to increase. Based on straight-ray reconstructions, Glide-Hurst et al. (2008) already established the feasibility of employing CURE sound-speed tomograms to estimate volumetric breast density. As a result, CURE sound-speed tomograms can be used to assess this breast cancer risk factor. Our *in vivo* study indicates that the TV bent-ray tomography algorithm can successfully image fatty and glandular tissue within the breast with higher resolution than the straight-ray algorithm (Fig. 5 through Fig. 8). As a result, we expect more accurate and better quantitative correlation between sound-speed and breast density in future studies. The illustrative example in Fig. 9 clearly shows the separation of fatty tissue (dark color) and breast parenchyma (light color) in our sound-speed tomograms. The four sagittal views are for breasts of different densities within the BI-RADS density categories 1-4. We can clearly see the increase of the breast parenchyma from fatty to dense breast. Moreover, there are a few advantages to use ultrasound sound-speed tomograms for breast density assessment: it is noninvasive, no breast compression is necessary, and the breast density is more accurate in volumetric (3-D) than 2-D projections. But the greatest advantage of UCT may be its non-ionizing density assessment, which will become very important when interventions such as hormonal or nutritional treatments are repeatedly monitored for potential reduction of breast cancer risk.

Another potential clinical application is to help detect and characterize breast lesions. Since most abnormal breast lesions have higher sound-speed than normal breast tissue (Gauss et al., 1997), UCT is a potential way to detect abnormal breast lesions. More importantly, our study

suggests greater detection of these elevated sound-speeds over the background for both malignant and benign breast lesions with the TV bent-ray algorithm. This further confirmed the feasibility of using sound-speed UCT to detect breast lesions, allowing higher contrast settings and improved threshold values for more prospective assessment of mass detection in the future. These more accurate sound-speed characterizations also applied to characterizing higher sound-speeds for malignant than benign lesions. One potential way to characterize a breast lesion is to compare a sound-speed tomogram with the corresponding CURE attenuation and reflection images. Statistically, the malignant lesions have elevated sound-speed and attenuation relative to surrounding tissue (Greenleaf et al., 1977). The architectural distortion at the tumor region in the reflection image is another indicator of cancer (Stavros et al., 1995). The addition of reflection and attenuation data can potentially further improve the separation of benign from cancer as illustrated in the color-coded fused image in Fig. 11. Studies based on such image fusions are undergoing in our group.

The third potential clinical application is to monitor clinical response of breast cancer patients to neo-adjuvant chemotherapy. Although chemotherapy is widely used to treat cancers, it is important to identify patients who are not responding to chemotherapy as early as possible, to avoid unsuccessful treatment strategies and unnecessary side effects (Rousseau et al., 2006; Tozaki, 2008). Accurate evaluation of a tumor's response to therapy is also necessary in order to plan for surgery (Partridge et al., 2002; Londero et al., 2004). In an ongoing study, we have used CURE images to monitor the progress of chemotherapy for 6 patients. CURE exams were performed at each cycle of chemotherapy. The sound-speed distribution from each scan was reconstructed to track the change in size, shape and mean sound-speed of the tumor. Compared to MRI, a significant potential advantage of using our sound-speed tomograms for chemotherapy

monitoring is the low cost for both patients and health care providers. Figure 12 illustrates our sound-speed tomograms, fused with CURE attenuation and reflection images, for one patient' chemotherapy monitoring, in which the change of the tumor size and shape during chemotherapy is demonstrated. Again, the greater potential accuracy of sound-speed measurements with the TV bent-ray algorithm and the ability to increase the contrast over the background makes this a more feasible procedure which could easily be automated and compared for patients at each follow-up visit over time.

There are several limitations in our study. First, the performance of our tomography algorithm declined when the lesion size dropped to and below the elevation beam width (5 mm for our ring array), since the signal dilution led to a loss of contrast. Another important factor influencing the performance of our algorithm is the signal-to-noise ratio of the acquired patient data. Although our in-house time-of-flight picker was tolerant to white noise, coherent noise in the ultrasound data might still affect the performance of the picker (Li et al., 2009). Thus, low signal-to-noise of the data might affect the accuracy of our time-of-flight picks. Consequently, bigger data errors would degrade the reconstructed sound-speed tomograms. Second, the trade-off between image resolution and computation speed needs to be balanced. For a typical breast scan with 76 slices, three-iteration inversion of the whole stack with 2 *mm* by 2 *mm* grid points on a 2.4 GHz Dell Precision workstation Duo Core (4 GB memory, redhat linux) required 1.5 hours to finish. If 1 *mm* by 1 *mm* grid size is used, the running time on the same computer is ~4 hours. Since most parts of our current algorithm implementation are sequential, the computation speed can be improved by parallelizing the code. Finally, the clinical implications suggest that it will be important to assess the relative contrast levels for algorithms in defining thresholds for viewing images on a prospective basis. Accurate depictions of local areas of increase sound-

speed may then become more reliable parameters for diagnostic assessment in clinical applications.

CONCLUSIONS

We developed a TV based bent-ray tomography algorithm for imaging the sound-speed distribution of the breast. We applied this algorithm to 61 breast datasets acquired using our clinical prototype CURE. Our sound-speed images showed that TV regularization, in combination with bent-ray tomography, better defined lesion edges and improved not only spatial resolution but significantly improved tissue contrast for better lesion conspicuity over background. Fatty and dense tissues could be well separated and mean sound-speeds of malignant lesions was higher than that of benign masses on average. Fusing sound-speed images with the corresponding attenuation and reflection images may help differentiate benign from malignant breast lesions. The lower costs compared to MRI and the lack of radiation exposure potentially allows UCT a prominent role in the future for therapeutic interventions, either for breast density deduction or cancer treatment.

Table 1. Comparison of sharpness of lesion edges for bent-ray and straight-ray reconstructions .

	Sharpness for bent-ray tomograms ($(m \cdot s)^{-1}$)	Sharpness for straight-ray tomograms ($(m \cdot s)^{-1}$)	Ratio
Figure 4 (fatty)	0.086	0.034	2.5
Figure 5 (scattered)	0.072	0.032	2.3
Figure 6 (hetero.)	0.102	0.049	2.1
Figure 7 (dense)	0.134	0.039	3.4

Table 2. Mean sound-speed with standard deviation (SD).

	Sound-speed (m/s)
Fat	1422 ± 9
Parenchyma	1487 ± 21
Malignant mass	1548 ± 17
Benign mass	1513 ± 27

Table 3. Mean sound-speed with standard deviation (SD).

	Mean sound-speed (m/s) (ROI selected by referring to reflection image)	Mean sound-speed (m/s) (ROI selected by thresholding)
Benign	1514 ± 34	1511 ± 14
Malignant	1549 ± 18	1546 ± 16

ACKNOWLEDGEMENTS

The authors wish to thank Lisa Bey-Knight for her help in recruiting patients and data collection. C. Li also wants to acknowledge Jason Shen for his assistance for the ROI segmentation of our images. This work was supported in part by research grant from the Michigan Economic Development Corporation (MEDC) and Susan G. Komen Breast Cancer Foundation. L. Huang also acknowledges the support of the U.S. DOE Laboratory-Directed Research and Development program at Los Alamos National Laboratory.

REFERENCES

ACRIN. Available at: http://www.acrin.org.

Andersen AH. Ray linking for computed tomography by rebinning of projection data. J. Acoust. Soc. Am. 1987;81:1190-1192.

Andersen AH. A ray tracing approach to restoration and resolution enhancement in experimental ultrasound tomography. Ultrasound Imaging 1990;12:268-291.

Andre MP, Janee HS, Martin PJ, Otto GP, Spivey BA, Palmer DA. High-speed data acquisition in a diffraction tomography system employing large-scale toroidal arrays. International Journal of Imaging Systems and Technology 1997;8:137-147.

Boyd NF, Byng JW, Jong RA, Fishell EK, Little LE, Miller AB, Lockwood GA, Tritchler DL, Yaffe MJ. Quantitative classification of mammograpic densities and breast cancer risk: Results from the Canadian National Breast Screening Study. J. Natl. Cancer Inst. 1995;87:670-675.

Boyd NF, Dite GS, Stone J, Gunasekara A, English DR, McCredie MR, Giles GG, Tritchler D. Chiarelli A, Yaffe MJ, Hopper JL. Heritabiligy of mammographic density, a risk factor for breast cancer. N. Engl. J. Med. 2002;347:886-894.

Carson PL, Meyer CR, Schezinger AL, Oughton TV. Breast imagin in coronal planes with simultaneous pulse echo and transmission ultrasound. Science 1981;214:1141-1143.

Chang CH, Huang SW, Yang HC, Chou YH, Li PC. Reconstruction of ultrasonic sound velocity and attenuation coeeficient using linear arrays: clinical assessment. Ultrasond in Med. & Biol. 2007;33:1681-1687.

Devaney A. Inverse scattering theory within the Rytov approximation. Opt. Lett. 1981;6:374-376.

Devaney A. Inverse formula for inverse scattering within the Born approximation. Opt Lett. 1982;7:111-112.

Duck FA, Physical prpperties of tissue. London: Academic Press, 1990.

Duric N, Littrup PJ, Babkin A, Chambers D, Azevedo S, Kalinin A, Pevzner R, Tokarev M, Holsapple E, Rama O, and Duncan R. Development of Ultrasound Tomography for Breast Imaging: Technical Assessment. Medical Physics 2005;32:1375–1386.

Duric N, Littrup P, Poulo L, Babkin A, Pevzner R, Holsapple E, Rama O, Glide C. Detection of breast cancer with ultrasound tomography: First results with the Computed Ultrasound Risk Evaluation (CURE) prototype. Medical Physics 2007;34:773-785.

Gauss RC, Soo MS, Trahey GE. Wavefront distortion measurements in the human breast. IEEE Ultraon Sympos 1997;2:1547-1551.

Glide CK, Duric N, Littrup P. Novel approach to evaluating breast density utilizing ultrasound tomography. Medical Physics 2007; 34:744-753.

Glide-Hurst CK, Duric N, Littrup P. Volumetric breast density evaluation from ultrasound tomography images. Medical Physics 2008; 35:3988-3997.

Greenleaf JF, Johnson A, Lee S, Harman G, Wood E. Acoustical Holography, N. Booth, Ed. (Plenum, New York) 1974;591-603.

Greenleaf JF, Johnson A, Bahn RC, Rajagopalan B. Quantitative cross-sectional imaging of ultrasound parameters. Ultrasounics Symposium Proceedings 1977;989-995.

Greenleaf JF, Bahn RC. Clinical imaging with transmissive ultrasonic computerized tomography. IEEE Transactions on Biomedical Engineering 1981;28:177-185.

Greenleaf JF, Litalo J, Gisvold JJ. Ultrasonic computed tomography for breast examination. IEEE Engineering in Medicine and Biology 1987;27-32.

Hansen PC. The L-curve and its use in the numerical treatment of inverse problems. Available at http://www.math/sintef.no/vskoler/2005/notes/Lcurve.pdf.

Hall FM. Mammographically Determined Breast Density and Cancer Risk. Radiology 2008;248:1083

Jego JR, Whittinghan TA. Experimental studies in transmission ultrasound tomography. Physics in Medicine and Biology 1991;36:1515-1527.

Jones HW. Recent activity in ultrasonic tomography. Ultrasonics 1993;31:353-360.

Johnson SA, Tracy ML. Inverse scattering solutions by a sinc basis, multiple source, moment method—part I: Theory. Ultrason. Imaging 1983;5:361-375.

Johnson SA, Borup DT, Wiskin JW, Natterer F, Wuebbling F, Zhang Y, Olsen C. Apparatus and Method for Imaging with Wavefields using Inverse Scattering Techniques. United States Patent 6,005,916 (1999).

Klimes L. Grid Travel-time Tracing: Second-order Method for the first Arrivals in Smooth Media. Pageoph 1996;148:539-563.

Kolb TM, Lichy J, Newhouse JH. Comparison of the Performance of Screening Mammography, Physical Examination, and Breast US and Evaluation of Factors that Influence Them: An Analysis of 27,825 Patient Evaluation. Radiology 2002;225:165-175.

Li C, Huang L, Duric N, Zhang H, Rowe C. An improved automatic time-of-fight picker for medical ultrasound tomography. Ultrasonics 2009;49:61-72.

Littrup PJ, Duric N, Azevedo S, Chambers DH, Candy JV, Johnson S, Auner G, Rather J and Holsapple ET. Computerized ultrasound risk evaluation (CURE) system: Development of combined transmission and reflection ultrasound with new reconstruction algorithms for breast imaging. Acoustical Imaging 2001;28:175-182.

Littrup PJ, Duric N, Leach Jr. RR, Azevedo SG, Candy JV, Moore T, Chambers DH, Mast JE and Holsapple ET. Characterizing tissue with acoustic parameters derived from ultrasound data. Proceedings of the SPIE: Medical Imaging 2002; San Diego, California; Feb. 23-28, 2002. Ultrasonic Imaging and Signal Processing – 4687-43.

Liu, DL, and Waag RC. Propagation and backpropagation for ultrasonic wavefront design. IEEE Trans. on Ultras. Ferro. and Freq. Contr. 1997;44:1-13.

Londero V, Bazzocchi M, Del Frate C, et al. Locally advanced breast cancer: comparison of mammography, sonography and MR imaging in evaluation of residual disease in women receiving neoadjuvant chemotherapy. Eur Radiol 2004; 14: 1371-1379.

Lucas-Fehm L. Sonographic mammographic correlation. Applied Radiology 2005 Feb;20-25.

Marmarelis VZ, Kim T, Shehada RE. Proceedings of the SPIE: Medical Imaging 2003; San Diego, California; Feb. 23-28, 2002. Ultrasonic Imaging and Signal Processing – Paper 5035-6.

Nocedal J, Wright SJ. Limited-Memory Quasi-Newton Methods: Numerical Optimization. Springer, 2nd ed. New York: Mikosch TV, Resnich SI, Robinson SM, 2000.

Norton SJ. Computing Ray trajectories between two points: A solution to the ray-linking problem. Optical Society of America 1987;4:1919-1922.

Partridge SC, Gibbs JE, Lu Y, Esserman LJ, Sudilovsky D, Hylton NM. Accuracy of MR imaging for revealing residual breast cancer in patients who have under gone neoadjuvant chemotherapy. AJR 2002; 179: 1193-1199.

Rousseau C, Devilliers A, Sagan C, Ferrer L, et al.. Monitoring of early response to neoadjuvant chemotherapy in stage II and III breast cancer by [18F] fluorodeoxyglucose positron emission tomography. JCO 2006; 24: 5366-5372.

Scherzinger AL, Belgam RA, Carson PA, Meyer CR, Sutherland JV, Bookstein FL. Assessment of ultrasonic computed tomography in symptomatic breast patients by discriminant analysis. Ultrasound in Med. And Biol. 1989;15:21-28.

Schomberg H. An improved approach to reconstructive ultrasound tomography. J. Phys. D: Appl. Phys 1978;11:L181-L185.

Schreiman J, Gisvold J, Greenleaf RB. Ultrasound transmission computed tomography of the breast. Radiology 1984;150:523-530.

Stvros AT, Thickman D, Rapp CL, Dennis MA, Parker MA, and Sisney GA. Solid breast nodules: use of sonography to distinguish between benign and maligmant lesions. Radiology 1995;196:123-134.

Tozaki M. Diagnosis of breast cancer: MDCT versus MRI. Breast Cancer 2008;15: 205-211.

Vogel CR, Oman ME. Fast, Robust Total Variation-Based Reconstruction of Noisy, Blurred Images. IEEE Transactions on Image Processing 1998;7:813-824.

Wolfe JN, Saftlas AF, Salane M. Mammographic parenchymal patterns and quantitative evaluation of mammographic densities: A case-control study. AJR, Am. J. Roentgenol. 1987;148:1087-1092.

FIGURE CAPTIONS

Fig. 1 The CURE clinical prototype. (a) Close-up of the imaging tank showing the transducer ring affixed to a mechanical arm that steps the ring down while imaging the entire breast volume; (b) A schematic representation of the CURE ring transducer. (From Duric et al 2007).

Fig. 2 Illustration of the grid model for forward modeling. Rays are traced from receiver to transmitter as shown in the figure.

Fig. 3 Comparison of TV (L1-norm) reconstruction in (a) with classic Tikhonov (L2-norm) reconstruction in (b). The breast has a 55 x 47 x 37 mm invasive ductal carcinoma at 12:00-1:00 o'clock. Those pixels inside the solid ellipse but outside the dashed ellipse are used to calculate the mean background sound-speed for (a) and (b),respectively. (c) Sound-speed cross-sections along the solid line in (a) and the dashed line in (b). (d) Segmented sound-speed image from (a). The left over pixels have sound-speeds high than background (1468 m/s) but lower than half power value (1530 m/s). (e) Segmented sound-speed image from (b). The left over pixels have sound-speeds high than background (1436 m/s) but lower than half power value (1501 m/s). The sound-speed scale in (a) and (b) is from 1350 m/s to 1468 m/s.

Fig. 4 ROI selection by referring to CURE reflection. (a) Sound-speed image showing an invasive ductal carcinoma at 12:00 to 1:00 o'clock. (b) ROI was manually selected in reflection image. (c) The ROI in (b) was applied to the image in (a) resulting the sound-speed image ith all 0's except that the original sound-speed values were unchanged within the ROI. (d) ROI selected by thresholding method.

Fig. 5 Sound-speed tomograms for a fatty breast that has a 21 x 17 x 20 (mm) fibroadenoma at 9:00-10:00 o'clock. (a) Sound-speed tomograms using bent-ray algorithm (third iteration); (b)

Sound-speed tomograms using straight-ray algorithm. (c) Upper panel: sound-speed along the solid line in (a). Lower panel: sound-speed along the dashed line in (b). The sound-speed scale in (a) and (b) is from 1350 m/s to 1550 m/s.

Fig. 6 Sound-speed tomograms for a breast with scattered fibroglandular tissue containing a 27 x 17 x 19 mm invasive ductal carcinoma at 2:00 o'clock. (a) Sound-speed tomograms using bent-ray algorithm (third iteration); (b) Sound-speed tomograms using straight-ray algorithm; (c) Upper panel: sound-speed along the solid line in (a). Lower panel: sound-speed along the dashed line in (b). The sound-speed scale in (a) and (b) is from 1350 m/s to 1550 m/s.

Fig. 7 Sound-speed tomograms for a heterogeneously dense breast with a 19 x 15 x 22 mm invasive ductal carcinoma at 10:00 o'clock. The lesion has incomplete margin as indicated in mammogram and US reports. (a) Sound-speed tomograms using bent-ray algorithm (third iteration); (b) Sound-speed tomograms using straight-ray algorithm. (c) Upper panel: sound-speed along the solid line in (a). Lower panel: sound-speed along the dashed line in (b). The sound-speed scale in (a) and (b) is from 1350 m/s to 1550 m/s.

Fig. 8 Sound-speed tomograms for a dense breast with a 16 x 11 x 18 mm fibroadenoma at 2:00 o'clock. (a) Sound-speed tomograms using bent-ray algorithm (third iteration); (b) Sound-speed tomograms using straight-ray algorithm. (c) Upper panel: sound-speed along the solid line in (a). Lower panel: sound-speed along the dashed line in (b). The sound-speed scale in (a) and (b) is from 1350 m/s to 1550 m/s.

Fig. 9 Sagittal views constructed from our sound-speed image stacks, for breasts of different densities corresponding to BI-RADS categories 1-4. (a) Fatty breast; (b) Scattered breast; (c) Heterogeneous breast; (d) Dense breast. For fair comparison, (a)-(d) are shown in the same

absolute sound-speed scale. Clearly, breast parenchyma increases from (a) to (d). The sound-speed scale in (a) and (b) is from 1350 m/s to 1550 m/s.

Fig. 10 Histogram of mean sound-speeds for 13 benign lesions (solid line) and 19 malignant lesions (dashed line).

Fig. 11 Color-coded fused image. (a) An invasive ductal carcinoma (high sound-speed and high attenuation); (b) the legend (reflection: red; sound-speed: green; attenuation: blue). Image contrast in (a) was adjusted to better illustrate breast lesion. CURE images are constructed from the same data, so they can be fused together without any geometric discrepancies.

Fig. 12 Clinical response of one breast cancer patient to neo-adjuvant chemotherapy shown in gray-scale fused images (sound-speed + attenuation +reflection) over a period of 8 weeks. The time resolution was 2 weeks.

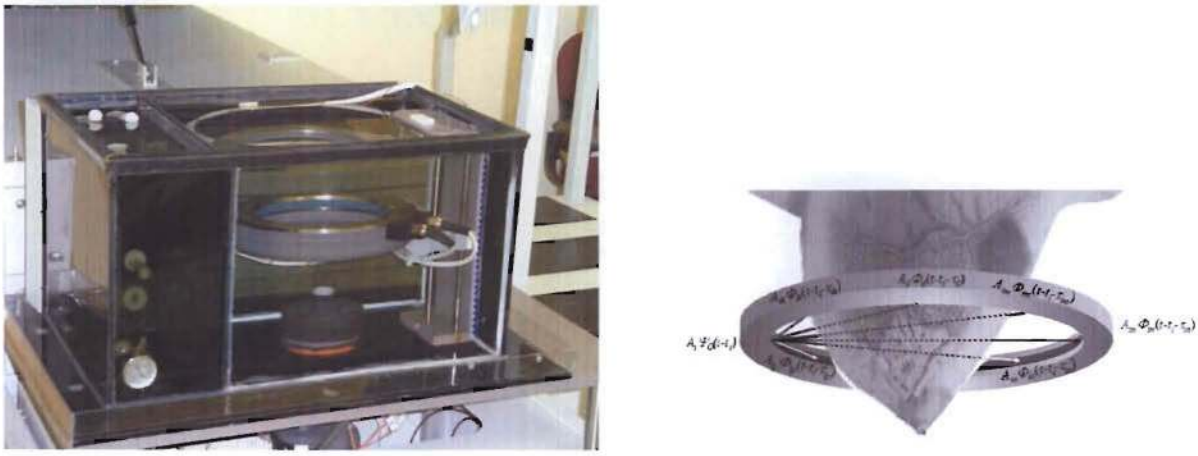

(a) (b)

Fig. 1 (from Duric et al 2007)

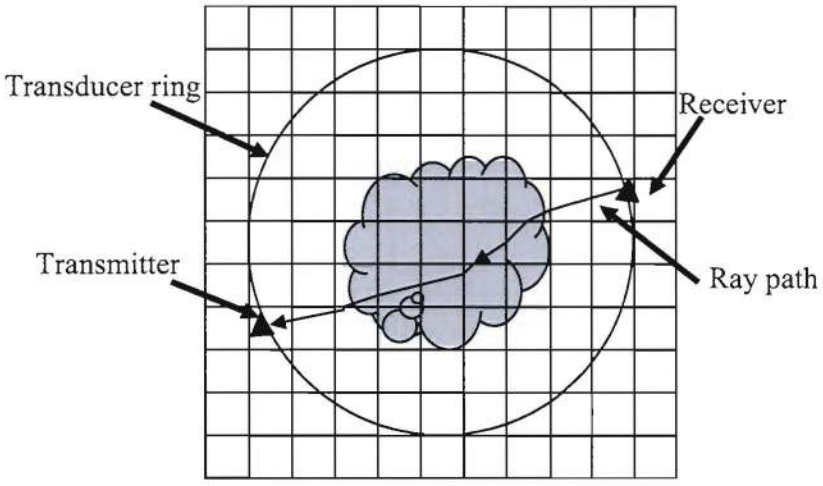

Fig. 2

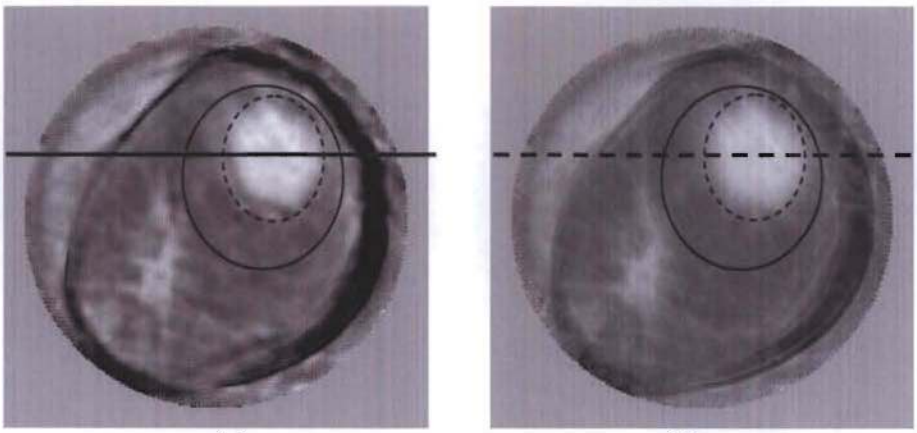

(a) (b)

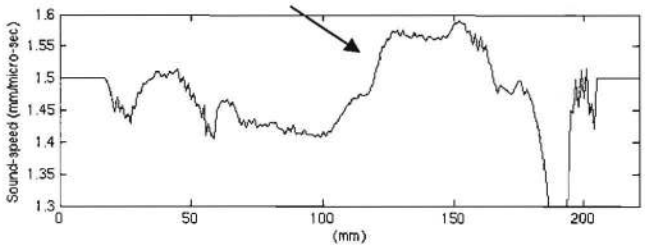
Sound-speed (mm/micro-sec)
1.6
1.55
1.5
1.45
1.4
1.35
1.3
0
50
100
150
200
(mm)

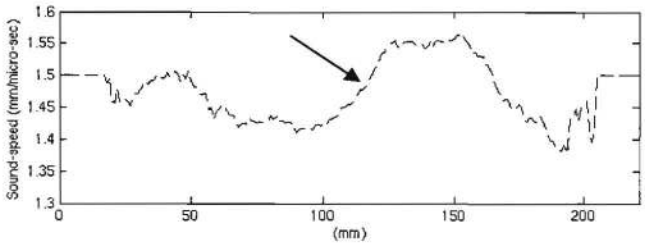
Sound-speed (mm/micro-sec)
1.6
1.55
1.5
1.45
1.4
1.35
1.3
0
50
100
150
200
(mm)

(c)

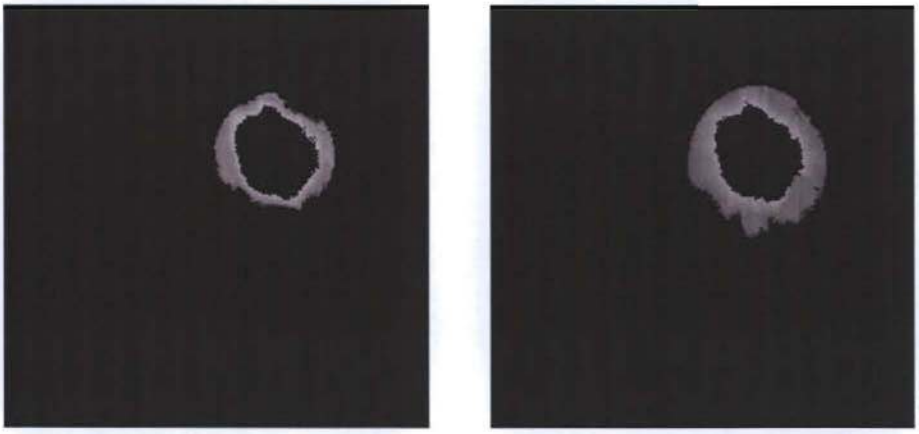

(d) (e)

Fig. 3

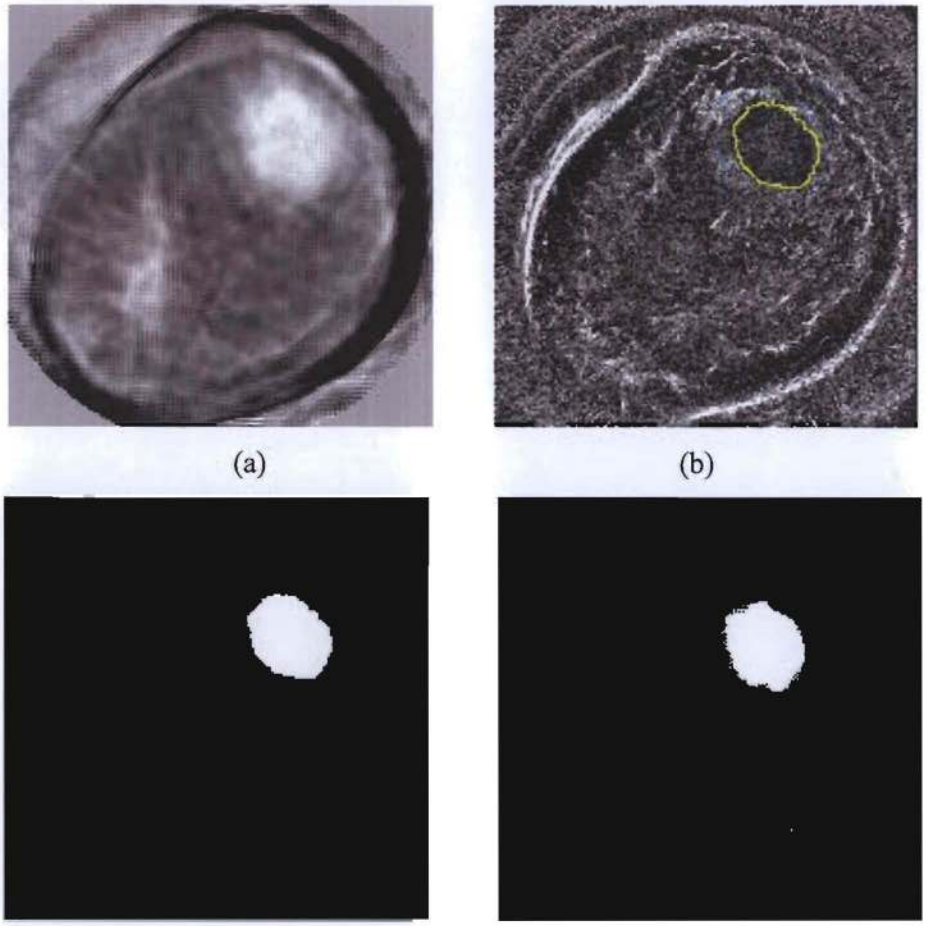

(a) (b)

(c) (d)

Fig. 4

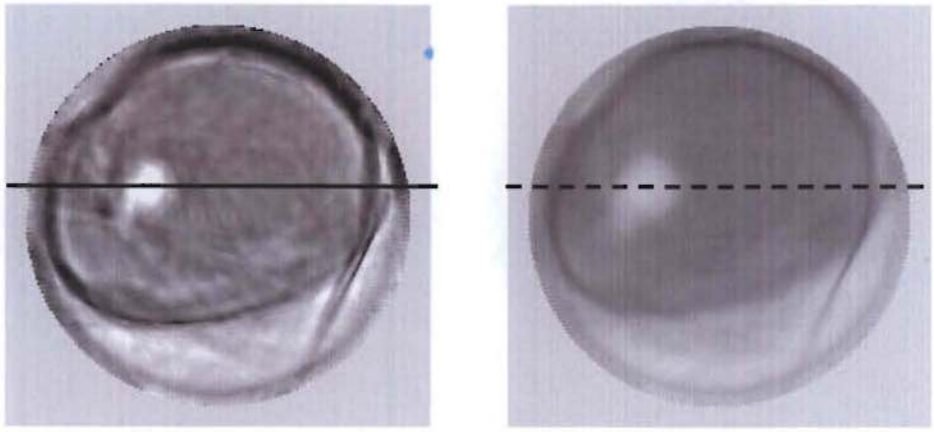

(a) (b)

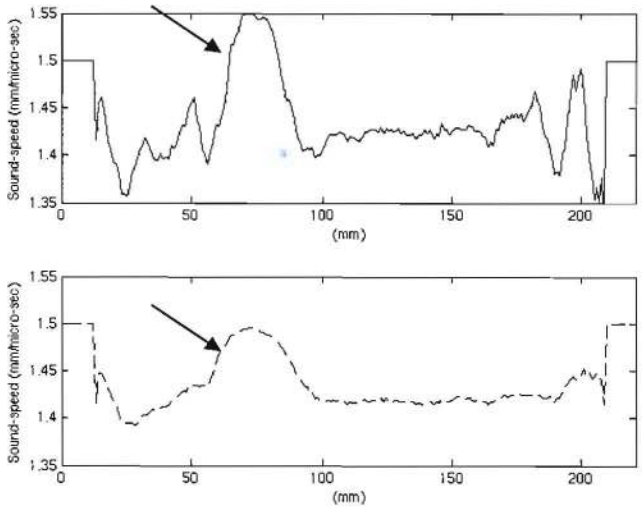
Sound-speed (mm/micro-sec)
1.55
1.5
1.45
1.4
1.35
0
50
100
150
200
(mm)
Sound-speed (mm/micro-sec)
1.55
1.5
1.45
1.4
1.35
0
50
100
150
200
(mm)

(c)

Fig. 5

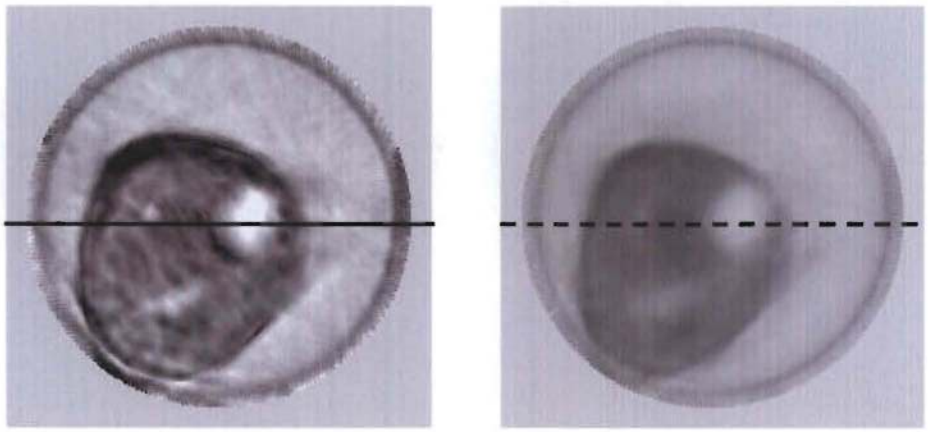

(a) (b)

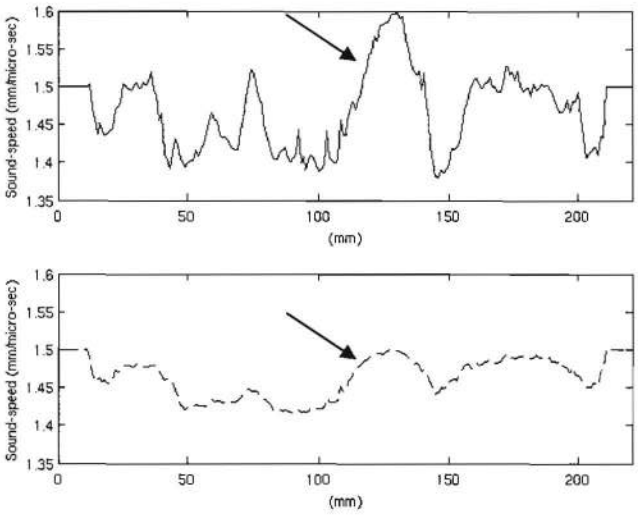
Sound-speed (mm/micro-sec)
1.6
1.55
1.5
1.45
1.4
1.35
0
50
100
150
200
(mm)
Sound-speed (mm/micro-sec)
1.6
1.55
1.5
1.45
1.4
1.35
0
50
100
150
200
(mm)

(c)

Fig. 6

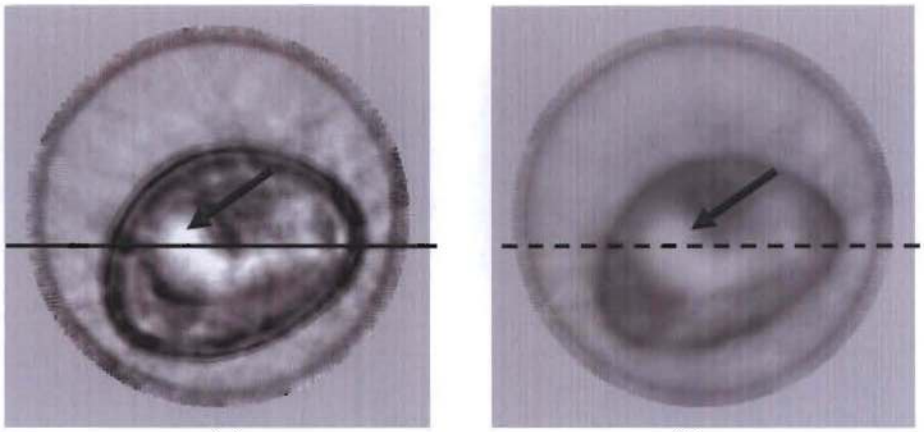

(a) (b)

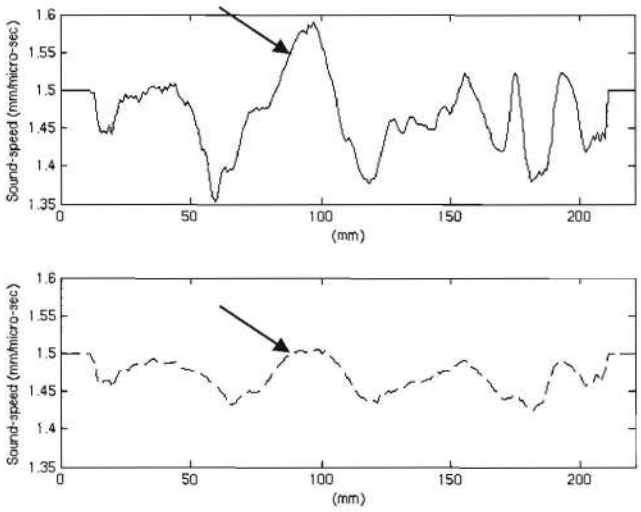

(c)

Fig. 7

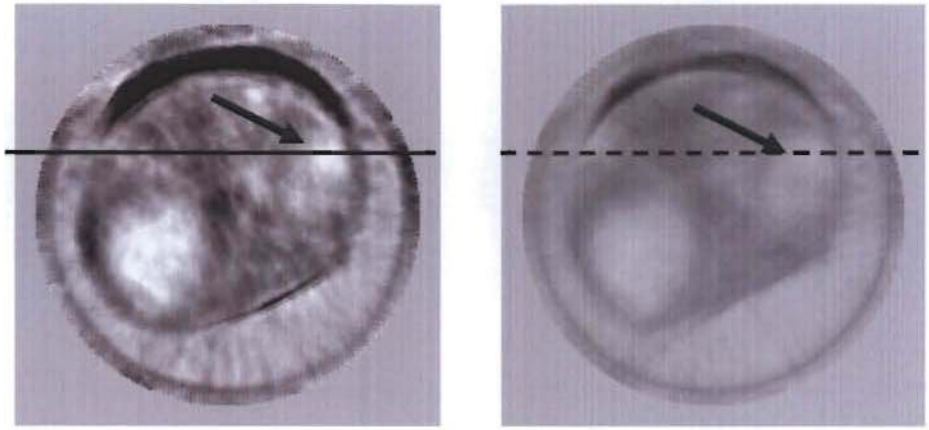

(b) (b)

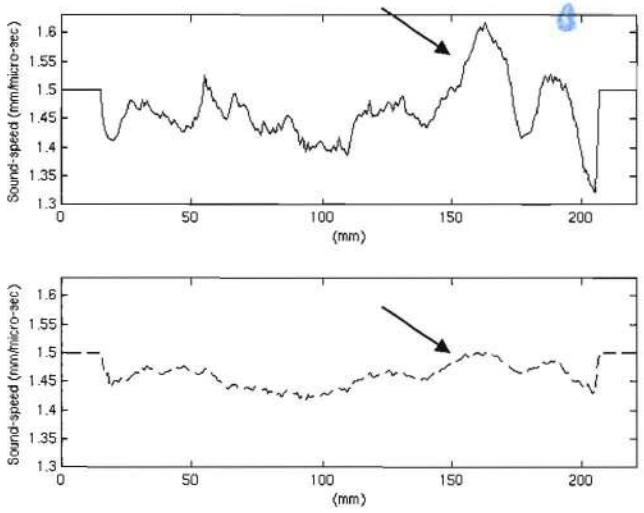
Sound-speed (mm/micro-sec)
1.6
1.55
1.5
1.45
1.4
1.35
1.3
0
50
100
150
200
(mm)
Sound-speed (mm/micro-sec)
1.6
1.55
1.5
1.45
1.4
1.35
1.3
0
50
100
150
200
(mm)

(c)

Fig. 8

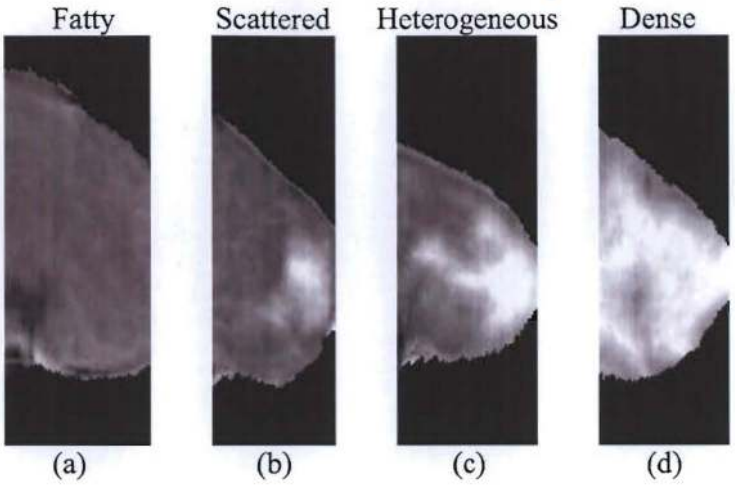
Fatty
Scattered
Heterogeneous
Dense
(a)
(b)
(c)
(d)

Fig. 9

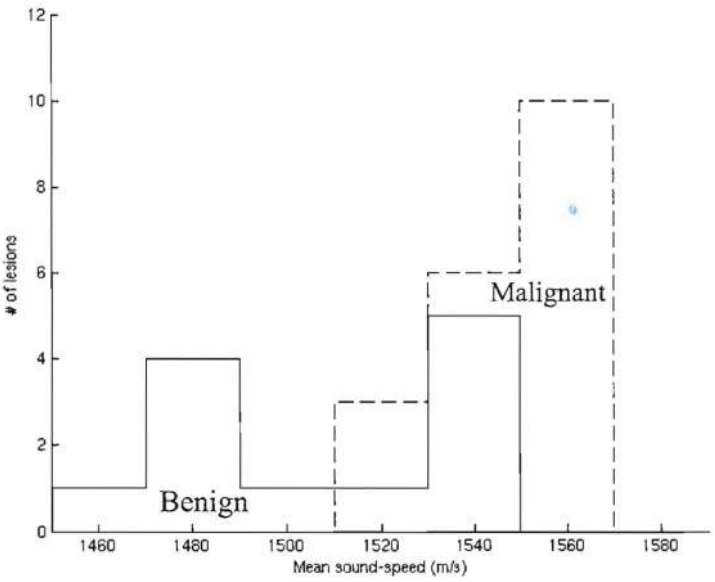
12
10
8
6
4
2
0
# of lesions
Malignant
Benign
1460
1480
1500
1520
1540
1560
1580
Mean sound-speed (m/s)

Fig. 10

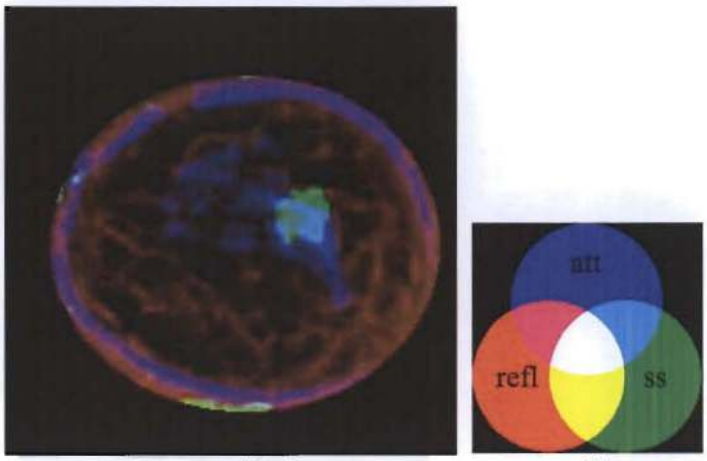

(a) (b)

Fig. 11

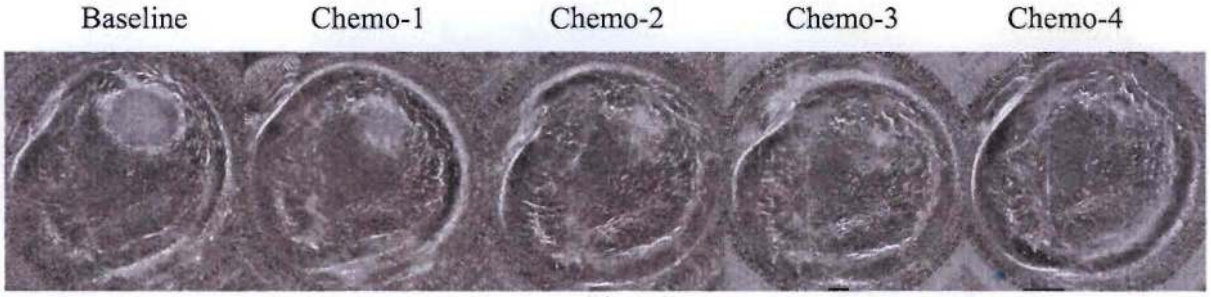

Fig. 12